JOURNAL OF AIRCRAFT
Vol. 47, No. 1, January–February 2010

Characteristics of Pitching and Plunging Airfoils Under Dynamic-Stall Conditions

D. Rival* and C. Tropea†
Technische Universität Darmstadt, 64287 Darmstadt, Germany

DOI: 10.2514/1.42528

An experimental investigation into the dynamic-stall process of a pitching and plunging airfoil at low Reynolds numbers has been carried out using direct force measurements and smoke visualization in an Eiffel-type wind tunnel. The strong influence of reduced frequency ($k = \pi fc/U_\infty$) on the vortical wake of both pure-plunging and pure-pitching airfoils is revealed. Here, a transition from a bluff body to a *mushroom*-type wake has been observed at approximately $k = 0.2$. Some associated lift and moment hysteresis curves for combined pitching and plunging motions are then presented with an accompanying discussion on the nature of the dynamic-stall process. For these complex motions, it is observed that both lift and moment phase lags grow with reduced frequency from $k = 0.05$ to 0.1. Despite substantial lift augmentation in the light- and deep-stall regimes, strong pitching-down moments are not avoided.

Nomenclature

c	=	airfoil chord
c_l	=	sectional lift coefficient
c_m	=	sectional moment coefficient
f	=	frequency
h	=	plunge position
h_o	=	plunge amplitude
k	=	reduced frequency, $\pi fc/U_\infty$
Re	=	Reynolds number, $U_\infty c/\nu$
T	=	period
t	=	time
U_∞	=	freestream velocity
u	=	streamwise velocity
x	=	streamwise direction
y	=	normal direction
z	=	spanwise direction
α	=	angle of attack
α_{eff}	=	effective angle of attack
$\alpha_{\max}$	=	angle of attack for maximum value
α_o	=	mean angle of attack
α_1	=	amplitude of angle of attack
ϕ	=	phase between pitch and plunge

I. Introduction

ACCOMPANIED with an ever-growing interest in micro air vehicle (MAV) development based on bioinspired flight (i.e., combined lift and propulsion from flapping wings) lies the challenging goal to scale down such vehicles to lower Reynolds numbers ($Re < 50,000$) [1]. In such low-Reynolds-number regimes, one of the major limitations is the separation-prone nature of the laminar boundary layer when faced with an adverse pressure gradient. Such a fundamental limitation on an airfoil's aerodynamics at these Reynolds numbers was investigated by Mueller and Batill [2] on a laminar profile using force measurements and smoke visualization. Several more recent studies have examined the transition to turbulence and the position of a laminar separation bubble for low angles of incidence and at $Re = 60,000$ [3]. Performance has been found to drop quite dramatically for $Re < 60,000$, where the transition and, therefore, reattachment occur even later, if at all. At such Reynolds numbers associated with cruise conditions, it is expected that lift must be generated through unsteady aerodynamic mechanisms such as dynamic stall [4], where the formation and delayed convection of a leading-edge vortex (LEV) over the downstroke can be very advantageous to lift production [5]. The importance of a spanwise flow for LEV stabilization has been the source of heated debates among biologists [6]. It is, however, not yet conclusive whether the spanwise flow found for large flapping amplitudes is an absolute requirement to stabilize the LEV, thus the selection of a simpler two-dimensional case in the present study. As an example of this two-dimensional stabilization, Thomas et al. [7] demonstrated that dragonflies produce large quasi-two-dimensional LEVs over their downstroke in cruise-flight conditions. Based on these aforementioned investigations and the inspiration from natural flight, an initial examination of the wake structure for various reduced frequencies ($0.05 < k < 0.3$) has been performed for the quasi-two-dimensional case specifically, to determine the level of unsteadiness and potential augmentation in lift attainable through dynamic stall.

II. Experimental Setup

The experimental rig consists of a base structure, a set of linear motors connected with each other via a linkage system, and a carbon-fiber SD7003 wall-spanning profile weighing 306 g. The profile has a chord length of 120 mm and a span of 450 mm. The profile-tip spacing at the walls is less than 2 mm on either side. The tunnel has a contraction ratio of 24:1 with five turbulence screens in the settling chamber, yielding turbulence levels under 0.5% at these low tunnel speeds of 3.75 and 7.5 m/s, corresponding to $Re = 30,000$ and 60,000, respectively. A schematic of the facility integrated into the Eiffel-type wind tunnel at the Institute of Fluid Mechanics and Aerodynamics (Technische Universität Darmstadt) is shown in Fig. 1.

The airfoil selected for this study is the asymmetric SD7003 profile, as it demonstrates relatively good performance in transitional Reynolds numbers. The profile has a maximum thickness of approximately $0.09c$ and a point of rotation located at the $x = c/4$ position. Another attractive feature when using the SD7003 profile is the substantial experimental database available in the open literature, both for the steady [3,8] and unsteady cases [9,10].

For the direct lift and moment measurements, a pair of one-component Kistler 9217A piezoelectric force sensors are integrated directly below the profile, one at the quarter-chord position (point of

Presented as Paper 0537 at the 47th AIAA Aerospace Sciences Meeting and Exhibit, Orlando, FL, 5–8 January 2009; received 3 December 2008; revision received 1 October 2009; accepted for publication 2 October 2009.

*Doctoral Researcher, Institute of Fluid Mechanics and Aerodynamics; currently Postdoctoral Associate, Mechanical Engineering, Massachusetts Institute of Technology, Cambridge, MA; rival@mit.edu.

†Professor, Institute of Fluid Mechanics and Aerodynamics.

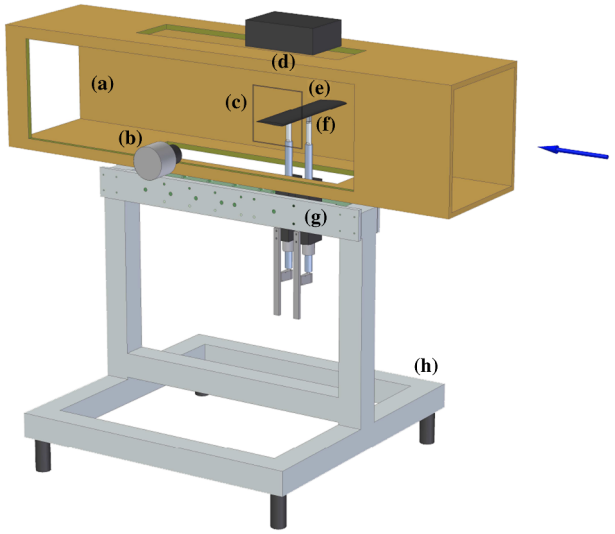

Fig. 1 Experimental setup in wind-tunnel test section with flow direction from right to left: a) test section, b) high-speed camera, c) image frame, d) light source, e) wall-spanning carbon-fiber profile, f) embedded piezoelectric force sensors, g) linear motors with linkage system, and h) base structure. Note that the gap in the tunnel floor is sealed for all tests.

rotation) and one at the trailing edge. Together, the two sensors can measure both the profile's inertial and aerodynamic forces during the prescribed movement. The total static tare weight of the system (profile and linkage combined) is 394 g. The analog-output charge signals from the two piezoelectric force sensors were sent through the wind-tunnel floor to a Kistler 5073A411 charge amplifier, which in turn converted the signals into an analog voltage. These voltage signals were subsequently fed into a 16-bit National Instruments 6259 A/D board. Since the physical and sting natural frequencies were on the order of 1 and 20 Hz, respectively, the signals were finally run through a 5 Hz low-pass filter in LabVIEW 8.2 and then further postprocessed using MATLAB 7.3. All lift and moment measurements were based on an ensemble of 30 clean cycles, sampled at 1 kHz, where the first four cycles as well as the last cycle were cut away due to aerodynamic and inertial starting and stopping effects. To subtract the dynamic tare for a given pitch–plunge case, a corresponding ensemble of 30 clean cycles was measured with the wind tunnel turned off. This technique proved to be very repeatable for the lower reduced frequencies ($k < 0.15$), for which the aerodynamic contribution was always equal to or larger than the inertial contribution. However, at higher reduced frequencies ($k > 0.2$), the inertial loads grew with the frequency squared and therefore very quickly dominated the total measured forces such that the accuracy of the results suffered greatly. Therefore, in this work, only direct force and moment measurements for lower reduced frequencies and at $Re = 60,000$ are presented, where the accuracy was estimated to lie within $\Delta C_l = \pm 0.05$ and $\Delta C_m = \pm 0.02$, respectively.

Smoke visualizations were performed by evaporating baby oil on an electrically heated, steel musical-instrument string of 0.16 mm in diameter, which was stretched vertically across the wind-tunnel test section. The heated wire was located at the quarter-span position, one chord upstream of the leading edge. High-speed images were recorded at 231 frames/second using a VDS Vosskühler HCC-1000 camera with a full resolution of 1024×1024 pixels coupled with a 50 mm $f1.2$ Nikkor lens. Illumination was performed using a 500 W halogen light source located directly above the plane of interest. Since the quality of the generated streaklines deteriorated at higher tunnel speeds, all smoke visualizations were performed at $Re=$ 30,000, corresponding to a tunnel speed of $U_\infty = 3.75$ m/s.

III. Parameter Space

A fully programmable control system was developed in LabVIEW, capable of communicating with the linear motors, and thus a full range of combined cyclic pitch/plunge motions could be achieved. Sinusoidal movements based on the following equations for pitch α and plunge h have been tested at plunge amplitudes of $h_o = 0.5c$ and frequencies up to $f = 3$ Hz, appropriate for the test-section size; note that for all investigations, the pitch motion led the plunge motion by $\phi = 90°$:

$$\alpha(t) = \alpha_o + \alpha_1 \cos(2\pi f t + \phi) \tag{1}$$

$$h(t) = h_o \cos(2\pi f t) \tag{2}$$

The effective angle of attack was defined in the following manner:

$$\alpha_{\text{eff}}(t) = \alpha_o + \alpha_1 \cos(2\pi f t + \phi) + \dot{h}/U_\infty + c\dot{\alpha}/2U_\infty \tag{3}$$

whereby the last term, often referred to as *dynamic cambering*, was neglected since its contribution was found to be minimal at these reduced frequencies. When comparing pure-pitching (simple oscillation in pitch) versus pure-plunging motions, a maximum phase advance of $0.04t/T$ in the effective angle-of-attack distribution for the pure-pitching case was observed for the most extreme case at $k = 0.25$. This discrepancy fell within the experimental error and was therefore ignored.

Varied were the angle-of-attack mean α_o and amplitude α_1 values, but always with a positive mean incidence, since the objective of the study was to look for lift augmentation through the dynamic-stall process. Also varied was the reduced frequency k, which was based on the airfoil chord length. The range of reduced frequencies examined in this study represents forward flight for most birds, bats, and large insects ($0.05 < k < 0.3$) [11]. Table 1 outlines the combined-motion (pitching and plunging) cases examined in this study.

IV. Initial Testing Under Static Conditions

Before dynamic measurements were performed, first a thorough comparison of static measurements were made with data available in the literature. In Fig. 2a static lift measurements at various plunge positions h in the test section corresponding to BDC (bottom dead center), center, and TDC (top dead center) were made to ascertain the levels of blockage in the tunnel. Based on these measurements, blockage effects were found to be negligible. However, it should be noted that stall did occur earlier in the experiment, when compared to the original measurements from Selig et al. [8]. To determine the level of three-dimensionality found in this configuration, surface oil-flow visualizations were made using a mix of baby oil and titanium dioxide. In Fig. 2b both the laminar separation s and turbulent reattachment r lines are visualized over the span of the airfoil for $\alpha_o = 4°$. It can be observed that as one moves from the center toward the tips of the profile that the laminar separation bubble shifts downstream. Furthermore, as one approaches the tip ($z = c/8$), the junction flow dominates and the separation and reattachment lines are no longer visible. However, under dynamic conditions, these wall-interference effects are expected to be greatly reduced. Some of the first experimental investigations into dynamic stall using a pitching airfoil [12] showed that the wing–wall interference became negligible as the reduced frequency approached $k \approx 0.1$. This was observed for tests with an aspect ratio of only 1.62, which is very low in contrast to the current investigation with an aspect ratio of 3.75. It also should be noted that at the center position of the model, the waviness of the separation line was found to be an artifact of the linear motors' magnetic field on the titanium dioxide powder. Nevertheless, the positioning of the struts is expected to have a local disturbance on the flowfield. Despite the above-mentioned

Table 1 Description of combined pitching and plunging cases tested

k	α_o	α_1
0.05	5, 10°	0, −5, −10°
0.1	5, 10°	2.5, −2.5, −7.5°

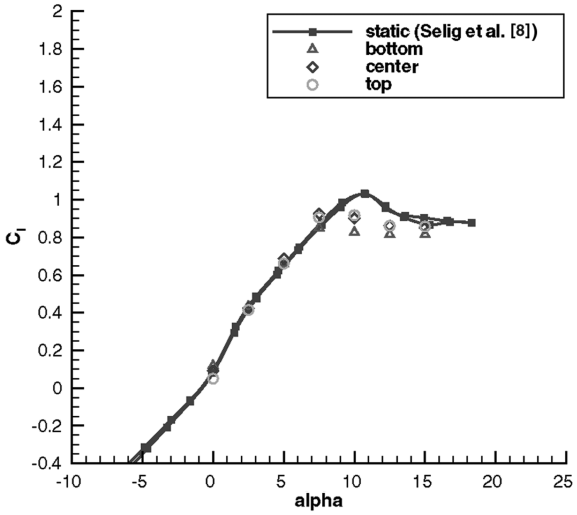

a) Static lift

b) Oil visualization at $\alpha = 4^{\circ}$

Fig. 2 Initial tests of SD7003 profile in tunnel at $Re = 60000$ under static conditions: a) static lift measurements in tunnel show little variation due to vertical positioning (i.e., blockage effects are small) and b) oil-flow visualization shows clear positioning of separation s and reattachment r lines, in agreement with previous experimental measurements made by Ol et al. [3].

disturbances (struts and walls), the overall bulk two-dimensionality of the flow is expected to be satisfied, and thus the integrated lift and moment measurements are representative of a pitching and plunging airfoil with infinite span.

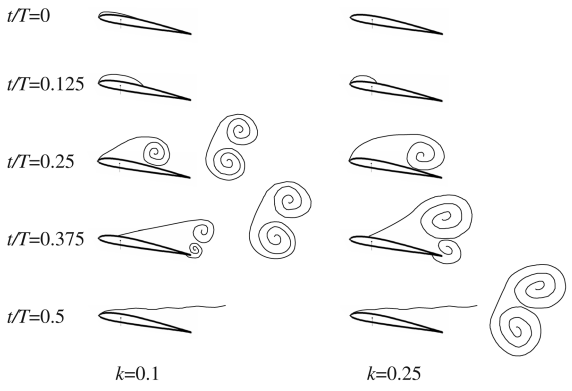

Fig. 3 Comparison of the wake formation during the downstroke for pure-plunging motions at two reduced frequencies with $\alpha_o = 8°$. Note that at the higher reduced frequency, a single, yet more distinct, vortex pair known as a mushroom structure is shed into the wake.

V. Results and Discussion

To first qualitatively investigate the nature of the dynamic-stall phenomenon and its associated wake, smoke-visualization studies were performed for various pure-plunging cases and for a range of reduced frequencies ($0.05 < k < 0.3$) at $\alpha_o = 8°$, where strong dynamic stall was evident. These studies elucidated the importance of the reduced frequency on the character of the wake when the plunge amplitude and geometric angle of attack were held constant. At lower reduced frequencies ($k < 0.15$) it was found that the dynamic-stall process and its associated shedding corresponded to a typical bluff-body-type von Kármán street with multiple alternating vortices shed from the leading and trailing edges. Up to four sets of such vortex pairs were shed over the downstroke. For higher reduced frequencies ($k > 0.2$), where the kinematic forcing was much more dominant, a single leading-edge and trailing-edge vortex pair was shed into the wake, forming a so-called *mushroom*-wake structure, as described by Panda and Zaman [13]. A qualitative sketch of these general differences in the wake is depicted in Fig. 3.

A. Pure-Pitching Versus Pure-Plunging Decomposition

The relative positioning of the shed vortices in the wake with respect to the airfoil is crucial to the lift and moment production, in that each shed vortex influences the strength of the bound vortex.

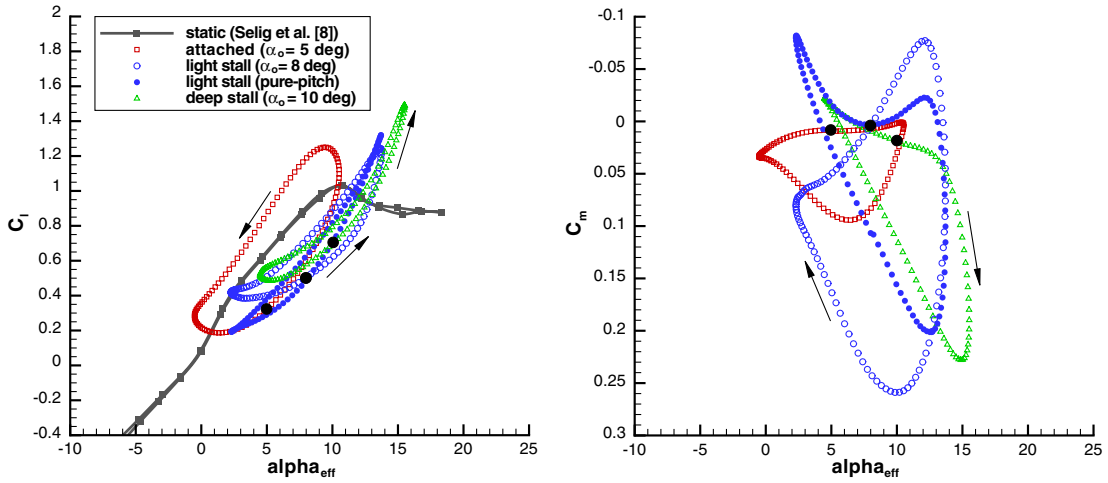

a) Lift hysteresis ($k = 0.1$)

b) Moment hysteresis ($k = 0.1$)

Fig. 4 Direct lift and moment coefficients for three pure-plunging cases ($\alpha_o = 5, 8$, and $10°$) and one equivalent pure-pitching case ($\alpha_o = 8°$) at $k = 0.1$. Note that the black circle represents the top of the stroke.

a) Plunge (k = 0.1) b) Pitch (k = 0.1) c) Plunge (k = 0.25) d) Pitch (k = 0.25)

Fig. 5 Comparison of equivalent pure-plunging and pure-pitching kinematics using smoke visualization with a mean angle of attack of $\alpha_o = 8°$. Note that sequences start at $t/T = 0$ (top of stroke) and follow in constant steps of $t/T = 1/16$. For $k = 0.1$ the effective angle of attack varies from top to bottom with $\alpha_{\text{eff}} = 8$, 10.2, 12.1, 13.3, 13.7, and 13.3°; for $k = 0.25$, the variation is $\alpha_{\text{eff}} = 8°$, 13.5, 18.1, 21.1, 22.1, and 21.1°.

This interaction is often referred to as the circulatory contribution. This vortex positioning has been further examined by comparing two cases with equivalent effective angle-of-attack time histories (pure plunging versus pure pitching). This comparison was made at two reduced frequencies with stall (differences in the attached flow regime are minimal): the first representative of bluff-body-type shedding ($k = 0.1$) and the second representative of mushroom-wake-type shedding ($k = 0.25$). For the bluff-body-type case, both lift and moment measurements were performed. It can be seen in Fig. 4a that the pure-plunging case exhibits a slightly larger aerodynamic lag

than the pure-pitching case, whereby the pure-pitching case demonstrates a larger peak-to-peak lift variation. When examining the moment distribution in Fig. 4b, the pure-pitching case demonstrates a much earlier recovery from moment stall, albeit with a strong overshoot into the pitch-up moment regime. This earlier recovery corresponds to the relative positioning of the shed LEV when compared to the pure-plunging case. When comparing these results with high Reynolds number measurements [4,12], a more gradual recovery from stall is observed here at these low Reynolds numbers, where the boundary-layer time scales are slower.

In Fig. 5, comparisons of the pure-plunging and pure-pitching vortical wakes were found to be qualitatively very similar. For the bluff-body-type case ($k = 0.1$) shown in Fig. 5a, the separation bubble is first visible at $t/T = 2/16$, whereby more pronounced for the pure-plunging case. In subsequent frames, the pure-plunging case tends to develop more quickly than the pure-pitching case, both in the streamwise and in the normal directions. The broader development of the wake in the normal direction is due to the quick downward movement of the airfoil in relation to the shed vortices. For the mushroom-type case ($k = 0.25$), again the first appearance of a separation bubble can be found at $t/T = 2/16$. From then on, the pure-plunging and pure-pitching cases share a nearly identical appearance.

B. Combined Motion

Direct force measurements for a combined pitching and plunging airfoil were performed as a means of examining the sensitivity of the main parameters such as reduced frequency k, mean angle of attack α_o, and amplitude of angle of attack α_1, as well as to better understand the lift-augmentation available through dynamic stall. A range of combined pitch and plunge motions were examined for two reduced frequencies: $k = 0.05$ and 0.1. Already at these relatively low reduced frequencies, strong hysteresis in both lift and moment coefficients were revealed. In both Figs. 6 and 7, with respective mean angles of attack of $\alpha_o = 5$ and 10°, the lift hysteresis curves change their sign of rotation from clockwise ($k = 0.05$) to counterclockwise ($k = 0.1$). This is explained by the aerodynamic phase lag, which grows with increasing reduced frequency. This phenomenon is explained by the strong influence of the shed vortices in the wake on the bound-airfoil circulation. Details of these unsteady (circulatory) effects are described in detail by Leishman [14] and Cebeci et al. [15] in the context of attached aerodynamics.

From both Figs. 6a and 7a, even at reduced frequencies as low as $k = 0.05$, clear signs of dynamic stall can be detected, observed as a strong lift overshoot beyond the peak static-stall lift value. This overshoot can be interpreted as an almost immediate adjustment of the pressure distribution to the incidence angle, accompanied by a lag in stall credited to the slow viscous time scale of the boundary layer; hence, the process is often referred to as *delayed stall*. A range of effective angle-of-attack variations and associated dynamic-stall regimes are plotted, representing *attached*, *light-stall*, *deep-stall*, and *very-deep-stall* cases, following the nomenclature of McCroskey's [4] studies on dynamic stall for pitching airfoils. These names refer to the level of separation encountered over the course of a given cycle. When examining the moment hysteresis curves, moment stall, as would be expected, is found to increase with deeper-stall conditions (seen as a sharp drop from the neutral moment condition), which is

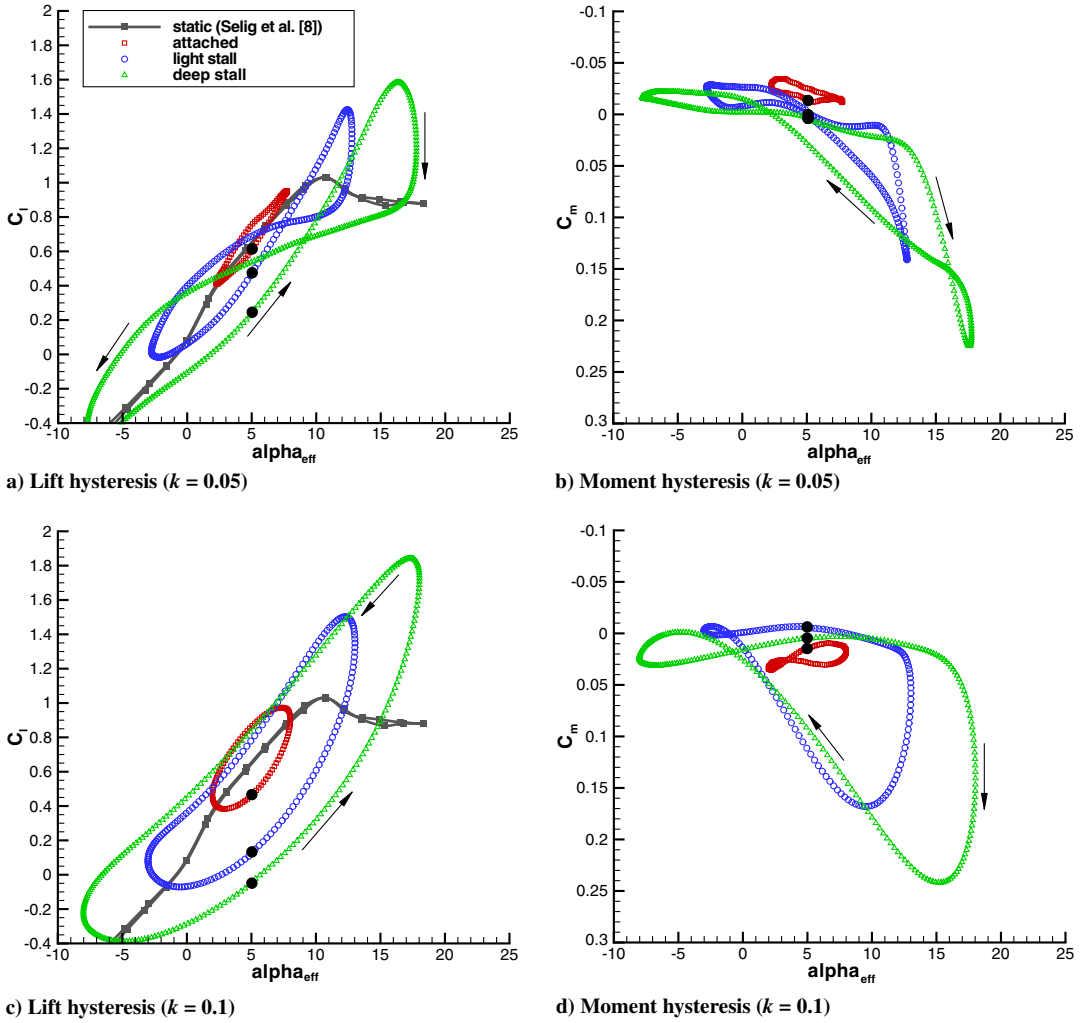

a) Lift hysteresis (k = 0.05)

b) Moment hysteresis (k = 0.05)

c) Lift hysteresis (k = 0.1)

d) Moment hysteresis (k = 0.1)

Fig. 6 Direct lift and moment coefficients for three effective angle-of-attack variations and a mean angle of attack of $\alpha_o = 5°$. Note that the black circle represents the top of the stroke.

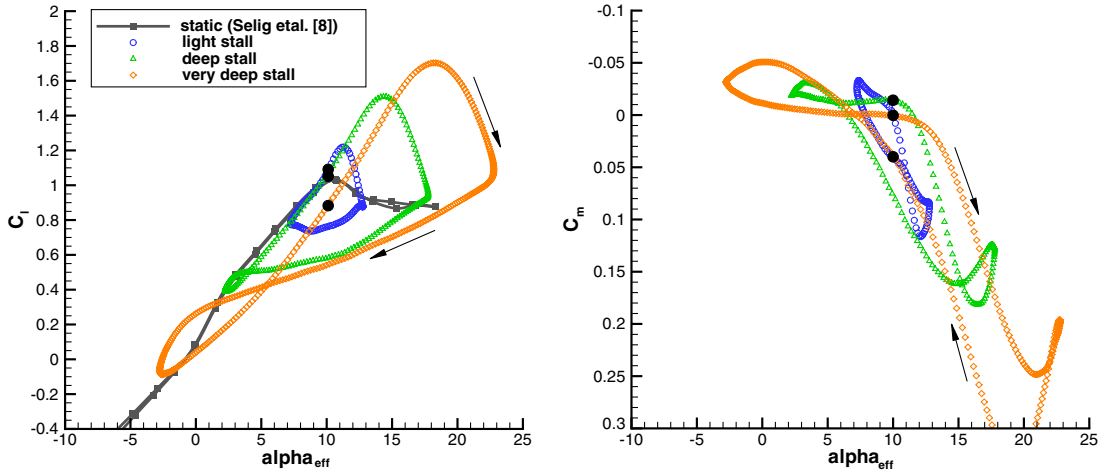

a) Lift hysteresis (k = 0.05)

b) Moment hysteresis (k = 0.05)

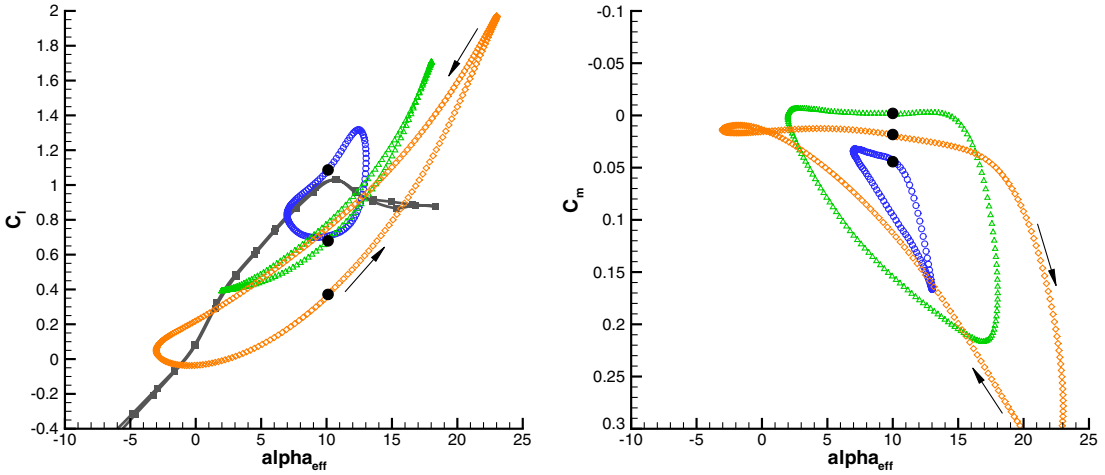

c) Lift hysteresis (k = 0.1)

d) Moment hysteresis (k = 0.1)

Fig. 7 Direct lift and moment coefficients for three effective angle-of-attack variations and a mean angle of attack of $\alpha_o = 10°$. Note that the black circle represents the top of the stroke.

clearly found when comparing Figs. 6b–6d, 7a, and 7b or Figs. 6d and 7a–7d with one another. This strong moment stall can be explained by the convection of the LEV along the airfoil surface. Once this low-pressure vortical structure passes the quarter-chord position, a strong pitch-down moment is generated until it sheds from the trailing edge, at which point the moment returns back to the neutral position. It can be seen for all cases that moment stall always occurs before lift stall. This is due to the fact that moment stall occurs as soon as the LEV moves aft of the point of rotation, whereas lift stall only occurs once the vortices are completely shed from the trailing edge.

When examining in more detail the moment hysteresis curves in Fig. 6, the ever-stronger nose-down pitching moment is explained by

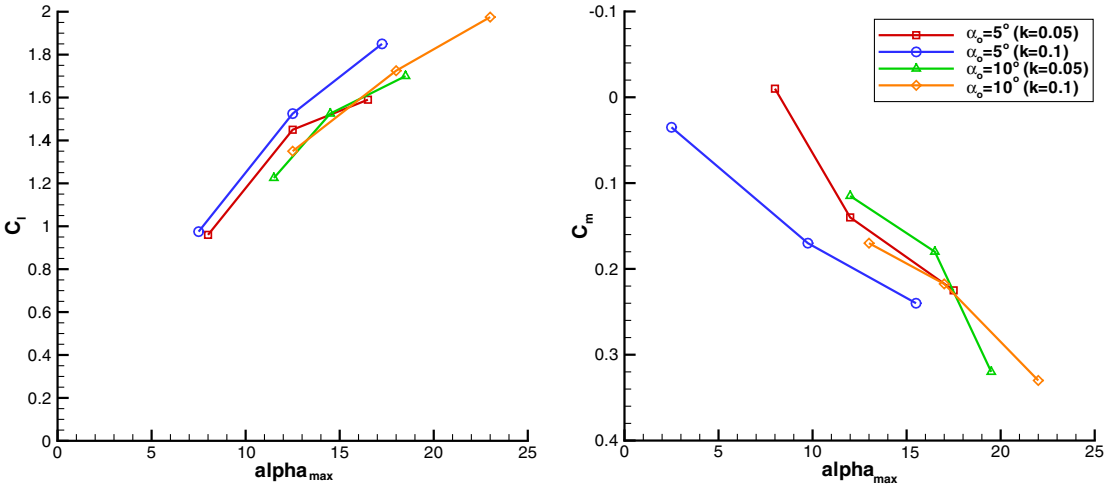

a) Peak lift

b) Peak moment

Fig. 8 Maximum lift and moment coefficients taken from Figs. 6 and 7.

the growing strength of the LEVs from light stall to deep stall, and even to very-deep-stall conditions. A further interesting feature to note is the difference in shape of the hysteresis curves between $k = 0.05$ and 0.1. In Fig. 6c counterclockwise lift loops are found, suggesting a much larger aerodynamic phase lag than for the lower reduced frequency of $k = 0.05$. This can be explained by the extra relative dwell time of the LEVs over the airfoil surface for the higher-reduced-frequency cases. Moving on to the deeper-stall cases in Fig. 7 with $\alpha_o = 10°$, one finds, as would be expected, an earlier stall during the downstroke (Fig. 7a) and even larger nose-down aerodynamic moments (Fig. 7b). At the higher reduced frequency of $k = 0.1$, peak lift is generated near the middle of the downstroke, representative of an aerodynamic phase lag of approximately $t/T = 0.25$, corresponding to a peak at the high effective angles of attack. The corresponding nose-down moments in Fig. 7d recover later in the upstroke when compared to the lower reduced frequency case in Fig. 7b. Despite the increase in hysteresis found for this higher mean angle of attack, peak lift is only marginally changed when compared to the deep-stall case in Fig. 6c. This suggests that as one moves deeper into stall, the potential of further lift augmentation diminishes, since the flowfield is no longer capable of reattaching on the upstroke.

A final comparison of the peak lift and moment coefficients for all combined pitch/plunge cases is made in Fig. 8. Here, it is found that the deep-stall case from Fig. 6c, with a reduced frequency of $k = 0.1$, shows very strong lift augmentation combined with a relatively low pitch-down moment. For the higher mean angle of attack of $\alpha_o = 10°$, there is a marginal improvement in lift, but at the price of a larger peak pitch-down moment. This suggests that lift augmentation in the light-stall regime is more effective than in the deep-stall regime, independent of kinematics (pitch or plunge), particularly at higher reduced frequencies.

VI. Conclusions

The effects of reduced frequency and angle of attack (both mean and amplitude) have been investigated for decomposed and combined pitching and plunging cases. A gradual transition from a bluff-body-type (multiple vortex pairs) to a mushroom-type wake is apparent at a reduced frequency of approximately $k = 0.2$. A comparison of pure-plunging and pure-pitching cases suggests that the equivalent flowfields are nearly identical and that variations in lift and moment are only a function of the shed-vortex positioning relative to the airfoil itself. For the combined pitch/plunge cases, the mean angle of attack α_o was found to be an important parameter, since it dictated, to a large extent, the level of dynamic stall found over the profile. When increasing from $k = 0.05$ to 0.1, the hysteresis curves were observed to switch from the clockwise to the counterclockwise directions, representing an increase in the total aerodynamic lag of approximately $t/T = 0.125$. Progressive increases in lift were achieved by moving from the stall onset to the light-stall regime and, finally, to the deep-stall regime. A slightly greater augmentation in lift (and aerodynamic lag) was generally found for the higher-reduced-frequency cases ($k = 0.1$). However, when operating at deep stall or beyond, large nose-down pitching moments (or moment stall) could not be avoided.

Acknowledgments

This research was supported by the Deutsche Forschungsgemeinschaft (DFG) within the national priority program entitled "Nature-Inspired Fluid Mechanics" (SPP1207). The authors would also like to thank the reviewers for their excellent feedback.

References

[1] Pines, D. J., and Bohorquez, F., "Challenges Facing Future Micro-Air-Vehicle Development," *Journal of Aircraft*, Vol. 43, No. 2, 2006, pp. 290–305.

[2] Mueller, T. J., and Batill, S. M., "Experimental Studies of Separation on a Two-Dimensional Airfoil at Low Reynolds Numbers," *AIAA Journal*, Vol. 20, No. 4, 1982, pp. 457–463. doi:10.2514/3.51095

[3] Ol, M. V., McAuliffe, B. R., Hanff, E. S., Scholz, U., and Kaehler, C., "Comparison of Laminar Separation Bubble Measurements on a Low Reynolds Number Airfoil in Three Facilities," 35th AIAA Fluid Dynamics Conference and Exhibit, AIAA Paper 2005-5149, Toronto, Canada, 2005.

[4] McCroskey, W. J., "Unsteady Airfoils," *Annual Review of Fluid Mechanics*, Vol. 14, 1982, pp. 285–311. doi:10.1146/annurev.fl.14.010182.001441

[5] Ellington, C. P., "The Novel Aerodynamics of Insect Flight: Applications to Micro-Air Vehicles," *Journal of Experimental Biology*, Vol. 202, No. 23, 1999, pp. 3439–3448.

[6] Ellington, C. P., "Insects Versus Birds: The Great Divide," 44th AIAA Aerospace Sciences Meeting and Exhibit, AIAA Paper 2006-35, Reno, NV, 2006.

[7] Thomas, A. L. R., Taylor, G. K., Srygley, R. B., Nudds, R. L., and Bomphrey, R. J., "Dragonfly Flight: Free-Flight and Tethered Flow Visualizations Reveal a Diverse Array of Unsteady Lift-Generating Mechanisms, Controlled Primarily Via Angle of Attack," *Journal of Experimental Biology*, Vol. 207, No. 24, 2004, pp. 4299–4323. doi:10.1242/jeb.01262

[8] Selig, M., Guglielmo, J., Broeren, A., and Giguere, P., *Summary of Low-Speed Airfoil Data*, SoarTech Publications, Virginia Beach, VA, 1995.

[9] Nerger, D., Kaehler, C. J., and Radespiel, R., "Zeitaufgeloeste PIV-Messungen an Einem Schwingenden SD7003-Profil bei $Re = 60,000$," *11 GALA Fachtagung*, Deutsche Gesellschaft für Laser-Anemometrie, Braunschweig, Germany, 2003.

[10] Lian, Y., Ol, M. V., and Shyy, W., "Comparative Study of Pitch-Plunge Airfoil Aerodynamics at Transitional Reynolds Number," 46th AIAA Aerospace Sciences Meeting and Exhibit, AIAA Paper 2008-0652, Reno, NV, 2008.

[11] Mueller, T. J., *Fixed and Flapping Wing Aerodynamics for Micro Air Vehicle Applications*, AIAA, Reston, VA, 2001.

[12] Carr, L. W., McAlister, K., and McCroskey, W., "Analysis of the Development of Dynamic Stall Based on Oscillating Airfoil Experiments," NASA TN D-8382, 1977.

[13] Panda, J., and Zaman, K. B. M. Q., "Experimental Investigation of the Flowfield on an Oscillating Airfoil and Estimation of Lift from Wake Surveys," *Journal of Fluid Mechanics*, Vol. 265, 1994, pp. 65–95. doi:10.1017/S0022112094000765

[14] Leishman, J. G., *Principles of Helicopter Aerodynamics*, 2nd ed., Cambridge Univ. Press, New York, 2006.

[15] Cebeci, T., Platzer, M., Chen, H., Chang, K., and Shao, J. P., *Analysis of Low-Speed Unsteady Airfoil Flows*, Springer, Heidelberg, Germany, 2005.